

# Land subsidence and ground fissures in Xi'an, China 2005–2012 revealed by multi-band InSAR time-series analysis



Feifei Qu<sup>a,c</sup>, Qin Zhang<sup>a,b</sup>, Zhong Lu<sup>c,\*</sup>, Chaoying Zhao<sup>a,b</sup>, Chengsheng Yang<sup>a</sup>, Jing Zhang<sup>a</sup>

<sup>a</sup> College of Geology Engineering and Geomatics, Chang'an University, No. 126 Yanta Road, Xi'an 710054, China

<sup>b</sup> Key Laboratory of Western China's Mineral Resources and Geological Engineering, Ministry of Education, No. 126 Yanta Road, Xi'an 710054, China

<sup>c</sup> Department of Earth Sciences, Southern Methodist University, Dallas, TX 75275, USA

## ARTICLE INFO

### Article history:

Received 21 May 2014

Received in revised form 28 July 2014

Accepted 4 September 2014

Available online 24 September 2014

### Keywords:

InSAR  
StaMPS SBAS  
Land subsidence  
Ground fissure  
Fault  
Geohazards  
Xi'an

## ABSTRACT

Xi'an, China has been undergoing significant land subsidence along with ground fissure development. These geohazards have brought about severe damages to buildings, bridges and other facilities. In order to warn of and mitigate disasters, it is urgently necessary to obtain the latest rate, extent, and temporal evolution of land subsidence in Xi'an. With multiple SAR datasets as well as leveling, GPS and ground water level of aquifers, we study and map the spatial and temporal evolution of land subsidence and ground fissures over Xi'an. First, 62 synthetic aperture radar (SAR) images acquired by Envisat, ALOS, and TerraSAR-X during 2005–2012 are used to form three independent interferometric stacks to unveil the spatial and temporal variations of land subsidence and ground fissures by using the time-series interferometric synthetic aperture radar (InSAR) technique. GPS and leveling measurements are applied to calibrate the InSAR results. Precision of our InSAR annual subsidence results is less than 9 mm. We derive the east–west and vertical components of the observed land deformation in 2009 using descending and ascending InSAR observations, finding out that the horizontal component of land deformation cannot be ignored if the deformation is large or ground fissures are active. Second, four main land subsidence zones are detected in Xi'an, with an average subsidence rate of 50 mm/a during 2005–2012. Time-series InSAR results indicate that land subsidence rates in Xi'an increased by 200% from 2005–2007 to 2008–2010, extending existing ground fissures. Third, InSAR-derived land subsidence correlates with the change in ground water level, and seasonal variations in subsidence correlate with changes in ground water pumping. Last, the consistency on the spatial–temporal distribution variation between ground fissures and land subsidence could be drawn from the time series results and profile analysis. Shapes of subsiding zones follow the general trends of mapped ground fissures and main faults in an ENE direction. Changes in the subsidence gradient are also observed over most of the ground fissures and faults. Subsidence-triggered fissures can cause localized surface displacements, aggravate localized subsidence, discontinue the integrity of ground water flow, and limit the horizontal spread of subsidence funnels. With continuing mass construction projects in Xi'an, monitoring ground deformation with satellite InSAR therefore can provide efficient means to image land subsidence, movements of fissures and faults, and the associated geohazards.

© 2014 Elsevier Inc. All rights reserved.

## 1. Introduction

Xi'an, the capital of Shaanxi Province, lies in the Wei River Basin over the northwestern China. The city of Xi'an (Fig. 1) is under a warm temperate semi-humid continental monsoon climate, with an average annual temperature of 12 °C and an annual precipitation of about 585 mm. Seasonal and inter-annual variations of precipitation are large, with the most amount in September and the least in December. The urban Xi'an is located to the north of the Qin Ling and south of the Loess Plateau, thus exhibiting both mountain and loess tableland landforms (Xi'an Local Records Compilation Committee, 1996; Zhuang,

Javed, Peng, & Liu, 2014). Because of the complex geological structures in Xi'an, plenty of natural geohazards, such as earthquakes, ground fissures, landslides and debris flows, frequently occurred in recent years. These geohazards have caused significant property damage and casualty loss in the Xi'an region (Chang'an University, 2009b; Xi'an Local Records Compilation Committee, 1996). Especially, due to urban sprawl and economic growth, Xi'an has been suffering severe land subsidence and ground fissure hazards since the 1960s. By the 1990s, areas with subsidence of more than 100 mm reached over 105 km<sup>2</sup> with the maximum subsidence reaching 1940 mm (Yan, 1998). The average rate of ground subsidence during the 1980s–1990s was 80–126 mm/a, with the maximum subsidence rate reaching 300 mm/a. Eight main subsidence funnels were formed in the southern, eastern and southwestern suburbs of Xi'an city, accompanied by 11 ground fissures

\* Corresponding author.

E-mail address: [zhonglu@smu.edu](mailto:zhonglu@smu.edu) (Z. Lu).

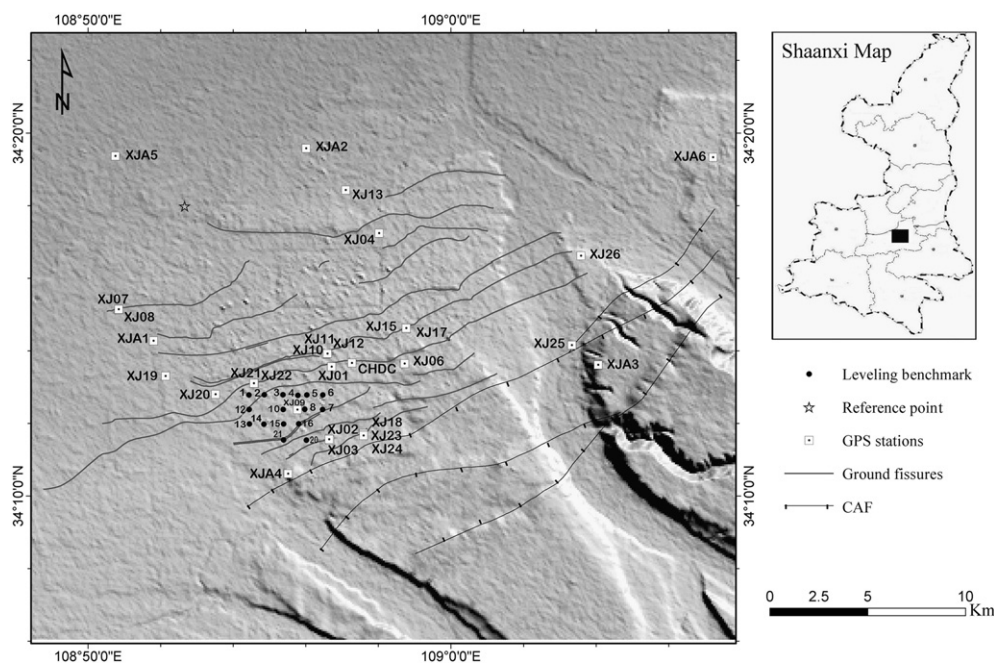


**Fig. 1.** Shaded relief map of Xi'an, where the Chang'an–Lintong fault (CAF), 14 ground fissures, leveling (black circles, numbers) and GPS benchmarks (with prefix XJ and marked by white squares) are superimposed. The map of Shaanxi Province is an inset on the top-right corner, where the black solid rectangle shows the study area of Xi'an.

oriented in an east–north–east (ENE) direction (Fig. 1). Several ellipsoidal subsidence cones with the major axes approximately parallel to the directions of ground fissures occurred between fissures (Lee, Zhang, & Zhang, 1996; Xi'an City Planning Bureau, 2006; Yan, 1999). The ground fissures are about 1–1.5 km apart, and generally parallel to the Chang'an–Lintong fault (CAF hereinafter), one of the main active faults in the region (Peng, Su, & Zhang, 1992).

Many geologists have studied the cause of land subsidence and ground fissure in Xi'an for several decades (e.g., Wang, 2000; Wang, Suo, & Jia, 1996). It has been concluded that the collaborative effect of the excessive exploitation of aquifer and the influence exerted by CAF is the main cause (Wang, 2000; Wang et al., 1996). Since 1995, most wells in the metropolitan area had been closed to reduce the land subsidence in Xi'an. However, obvious land subsidence was still recorded by step leveling, and three new ground fissures were discovered during 2001–2003 (Suo, Wang, & Liu, 2005). Moreover, spatially varied land settlements have exacerbated movements of ground fissures. So to date, a total of 14 fissures (see Fig. 1) have been mapped in Xi'an city. Land subsidence and induced ground fissure have caused immense damages to underground pipelines and other infrastructures (Chang'an University, 2009a,b, 2012). With the purpose of disaster prevention, mitigation and warning, it is urgent to obtain the latest rate, extent, and temporal evolution of land subsidence in Xi'an.

Ground-based techniques (e.g., leveling, GPS) have been utilized to investigate the land subsidence in Xi'an (Yan, 1998, 1999; Zhang et al., 2009; Zhu, Cheng, & Jiang, 2005; Zhu, Wang, Tian, Liang, & Zhang, 2006). Leveling measurements were conducted from 1959 to 1995. GPS campaigns have been surveyed biannually since 2005 (Chang'an University, 2009a, 2012) (Fig. 1). Since 2009, a total of 33 leveling benchmarks have been gradually installed and surveyed annually over the fast-developing region at Xi'an High-tech Zone in western Xi'an (Fig. 1). Even though ground-based monitoring techniques provide high-accuracy surface subsidence measurements at selected locations, they have difficulties in providing a more detailed and comprehensive picture of the ground deformation. Since the mid-1990s, InSAR has become a very useful remote sensing tool for mapping ground deformation due to earthquakes, volcanoes, landslides, land subsidence, etc. (Lu & Dzurisin, 2014; Lu et al., 2003; Massonnet et al., 1993; Schmidt & Bürgmann, 2003; Zebker, Rosen, Goldstein, Gabriel, & Werner, 1994).

The conventional InSAR method was applied in the earlier years to investigate land surface subsidence based on individual interferograms (Amelung, Galloway, Bell, Zebker, & Lacznik, 1999; Bawden, Thatcher, Stein, Hudnut, & Peltzer, 2001; Hoffmann, Zebker, & Galloway, 2001; Lu & Danskin, 2001; Peltzer & Rosen, 1995). However, the spatial and temporal decorrelation between SAR acquisitions often makes InSAR less robust (e.g., Zebker & Villaseno, 1992). In addition, the accuracy of InSAR measurements can be significantly reduced by atmospheric phase artifacts and orbital errors (Ferretti, Prati, & Rocca, 2001). Accordingly, advanced multi-interferogram InSAR techniques such as Persistent Scatterers InSAR (PSInSAR) and Small Baseline Subset (SBAS) InSAR have been developed to map time-series land surface displacements by minimizing artifacts plaguing the conventional InSAR method (Berardino, Fornaro, Lanari, & Sansosti, 2002; Ferretti et al., 2011, 2001; Hooper, Zebker, Segall, & Kampes, 2004; Lu, Dzurisin, Jung, Zhang, & Zhang, 2010; Lu & Zhang, 2014; Mora, Mallorqui, & Broquetas, 2003; Werner, Wegmuller, Strozzi, & Wiesmann, 2003). Multi-interferogram InSAR technique has facilitated the monitoring of land subsidence in many urban areas, such as Las Vegas (Burbey, 2002), Paris (Fruneau & Sarti, 2000), Naples (Tesauro et al., 2000), Mexico City (Osmanoglu, Dixon, Wdowinski, Cabral-Cano, & Jiang, 2011), Granada Basin (Joaquim, Hooper, Hanssen, Bastos, & Ruiz, 2011), Lisbon (Heleno et al., 2011), Hong Kong (Ding, Liu, Li, Li, & Chen, 2004), Shanghai and Tianjin (Perissin & Wang, 2010). In this manuscript, we utilize a multi-interferogram processing method – Stanford Method for Persistent Scatterers (StaMPS) SBAS (Hooper, 2008) – to investigate land subsidence over Xi'an, China. StaMPS SBAS uses the spatial correlation of interferometric phase measurements to identify pixels with low phase variance. StaMPS SBAS has an advantage over other multi-interferogram processing techniques as it can operate on single-look images to identify individual phase-coherent pixels surrounded by completely decorrelated pixels. Prior knowledge of temporal variations in the deformation rate over the study region is not required.

Regarding land subsidence and ground fissure monitoring in Xi'an using InSAR technique, some annual InSAR deformation results have been presented in recent years (Zhang et al., 2009; Zhao, Zhang, Ding, Peng, & Yang, 2008; Zhao et al., 2009). Zhang et al. (2009) studied the land subsidence and ground fissure activities during 1992–2006 by using both GPS and InSAR observations. Zhao et al. (2008, 2009) studied

the evolution of land subsidence during 1992–2007 by using 15 ERS 1/2 and Envisat scenes and land subsidence during 2005–2006 by using seven frames of Envisat data. Some GPS data were used to validate the InSAR results and centimeter precision was achieved. The above literatures identified main land subsidence stages in 1992, 1996, 2004, 2005 and 2006, and the changes in distribution and magnitude of the subsidence. The land subsidence and ground fissures have gradually extended to the south, southwest, and southeast suburbs of the city along with the expanding Xi'an Hi-tech Zone construction. The maximum land subsidence rates increased from 1992 to 1996 and then decreased until 2005, mainly owing to the 1996 policy of controlling underground water withdrawal. There has been no new research on ground subsidence and fissure activity in Xi'an since 2006. In addition, all of the above InSAR results were carried out by the conventional D-InSAR method, so ground displacement signals were possibly mixed with noise due to variations in atmospheric conditions and errors in satellite orbit and digital elevation model (DEM). To obtain the latest rate, extent, and temporal evolution of land subsidence in Xi'an, new data and more advanced InSAR processing approaches are needed.

With multiple SAR datasets as well as leveling and GPS measurements in Xi'an since 2005, this paper investigates the spatial and temporal evolution of land subsidence in Xi'an using advanced InSAR measurements (Hooper, 2008; Hooper & Zebker, 2007; Hooper et al., 2004). First, time series deformation measurements from 2005 to 2012 are generated by integrating X-, C-, and L-band interferograms to unveil the temporal and spatial variations of land subsidence in Xi'an. Together with the subsidence results of the 1990s (Zhang et al., 2009; Zhao et al., 2008, 2009), spatial-temporal variations of land subsidence in Xi'an over nearly twenty years can be achieved. Second, GPS and leveling measurements are applied to validate our InSAR results, while cross-validation of deformation measurements from ascending L-band ALOS and descending C-band Envisat datasets in 2009 is conducted. Third, horizontal and vertical components of motion during 2009 are derived based on ascending- and descending-track InSAR measurements. Fourth, the cumulative subsidence from 2005 to 2012 is obtained using three InSAR datasets, and its correlation with ground fissures and active faults is analyzed. Finally, causes of land subsidence and ground fissure movements as well as their interactions are discussed. The rest of the manuscript is organized as the following: Section 2 introduces the StaMPS SBAS algorithm as well as the data used for processing and validation, Section 3 includes the results of time-series land subsidence in Xi'an achieved by multi-band SAR data and their accuracy assessment, Section 4 presents the spatial-temporal variations of land subsidence as well as their correlation with ground-water pumping and activities of ground fissures and faults, and Section 5 summarizes our conclusions.

## 2. Datasets and processing methods

### 2.1. GPS and leveling measurements

A GPS network composed of 31 benchmarks (Fig. 1) constructed in 2005 has been surveyed biannually: 6 stations (labeled as XJA1–XJA6) are set as base stations and the other 25 stations (labeled as XJ01–XJ25) are set as monitoring points. The leveling measurements over the Xi'an High-tech Zone started in late 2009, including a total of 33 leveling benchmarks operated at different periods. 16 leveling benchmarks were in operation in 2012 (Fig. 1). The precisions of GPS vertical components and leveling measurements are about 5 mm and 2 mm, respectively (Zhang et al., 2009).

### 2.2. SAR data

SAR images from three different sensors with different imaging geometries are obtained for this study. The C-, L-, and X-band data information used at Xi'an is listed in Table 1.

**Table 1**

The C-, L-, and X-band SAR data information used in this study.

Sensor	Envisat ASAR	ALOS PALSAR	TerraSAR-X
Band	C	L	X
Wavelength (cm)	5.6	23.6	3.1
Heading (°)	−165.6	−10.2	−169.3
Incidence angle (°)	23.2	38.7	28.6
Track	161	464	13
Polarization	VV	HH, HV	HH
Number of images	27	20	15
Date range	2005.01.29– 2010.09.25	2007.01.30– 2011.02.10	2011.10.05– 2012.09.21

### 2.3. SBAS method

SBAS InSAR analysis technique relies on adequate combinations of multiple small baseline interferograms to increase the temporal sampling rate (e.g., Berardino et al., 2002; Lanari et al., 2004; Lee, Lu, Jung, Won, & Dzurisin, 2010; Wegmuller, Walter, Spreckels, & Werner, 2010). Standard SBAS methods often work with interferograms that are normally multilooked, filtered, and unwrapped individually (Berardino et al., 2002). SBAS operation in Stanford Method for Persistent Scatterers (StaMPS) (Hooper, 2008) can work on single-look images to identify single-look slow-varying filtered phase (SFP) pixels, whose phases decorrelate little over short time intervals. This offers the potential to operate SBAS processing at the highest spatial resolution, enabling the identification of isolated SFP pixels surrounded by completely decorrelated pixels (Hooper, 2008; Hooper & Zebker, 2007).

To maximize InSAR coherence, the StaMPS SBAS technique forms interferograms by taking into account the difference in Doppler frequency and spatial baseline as well as time interval of the image pair (Hooper, 2008). Here we select interferograms whose temporal, perpendicular and Doppler baselines are below the given threshold values (Hooper, 2008). The interferograms are formed by spectrum filters to remove non-overlapping Doppler spectra in the azimuth direction and to reduce the geometric decorrelation in the range direction. The flat-Earth and topographic phases are subtracted for each small-baseline interferogram based on 3-arc-second SRTM DEM. StaMPS SBAS uses the statistical relationship between amplitude stability and phase stability, which makes consideration of backscattering amplitude for reducing the initial number of pixels for phase analysis (Hooper, 2008; Hooper et al., 2004). After subsets of pixels are selected as initial SFP candidates, their phase stabilities are estimated under the assumption that the ground displacement is spatially correlated. The spatially-correlated contributions to the interferometric phase at a SFP candidate pixel, including phase components due to the ground displacement, the temporal change in atmospheric delay, the orbital inaccuracy and the spatially-correlated height error, are estimated by band-pass filter applied in the frequency domain of surrounding pixels. The spatially-uncorrelated contributions, including phase components due to both the spatially-uncorrelated height error and the deviation of the pixel's effective phase center from its physical center (i.e., spatially-uncorrelated look angle error), are then estimated through their correlation with the perpendicular baseline. Subtraction of these two estimates (i.e., the spatially-correlated and spatially-uncorrelated terms) from the interferometric phase leaves an estimate of the decorrelation noise,  $\gamma_x$ , which is a representation of variations in the residual phase at the SFP candidate pixel (Hooper, 2006, 2008; Hooper & Zebker, 2007; Hooper et al., 2004):

$$\gamma_x = \frac{1}{N} \left| \sum_{i=1}^N \exp \left\{ \sqrt{-1} \left( \psi_{x,i} - \Delta \hat{\psi}_{\theta,x,i}^u - \tilde{\psi}_{x,i} \right) \right\} \right| \quad (1)$$

where  $N$  is the number of interferograms,  $\psi_{x,i}$  is the wrapped phase of pixel  $x$  in the  $i$ th interferogram,  $\hat{\psi}_{\theta,x,i}^u$  is the estimated spatially-uncorrelated look angle error term and  $\tilde{\psi}_{x,i}$  is the estimate of the spatially-correlated term.

The root-mean-square change in  $\gamma_x$  (Eq. 1) is calculated at each iteration. When the change ceases to decrease, the solution has converged and the iteration stops. A threshold value of  $\gamma_x$ , which is calculated based on the maximum acceptable percentage of misidentified SFP pixels, is used for the selection of final SFP pixels (Hooper, 2008; Hooper, Segall, & Zebker, 2007).

Once SFP pixels have been selected, the phase at each SFP location is corrected using the estimate of spatially-uncorrelated look angle error calculated in the selection steps. Then, StaMPS SBAS uses the network flow approach to conduct three-dimensional phase unwrapping on multiple-master time-series interferograms (Hooper & Zebker, 2007). Afterwards, a low-pass filter in space and a subsequent high-pass filter in time can be applied to the unwrapped interferometric phases in order to remove the remaining spatially correlated errors related to orbit and atmosphere artifacts (Hooper, 2008; Hooper et al., 2007). Finally, time-series deformation measurements at each SFP location can be obtained.

Under the above criteria, we construct a total of 147 interferograms including 52 from C-band Envisat, 50 from L-band PALSAR and 45 from X-band TerraSAR-X (Fig. 2). Several interferograms with temporal/spatial baselines larger than the thresholds are also included to guarantee temporal continuity for SBAS time-series analysis (Fig. 2). The Doris software (Kampes, Hanssen, & Perski, 2003) is used for the interferometric processing. Each slave image is resampled to the master geometry and corrected for the difference in position of the master and slave sensor, using the WGS84 reference ellipsoid. The three datasets were then processed using the above StaMPS SBAS method respectively.

### 3. Results and analyses

#### 3.1. Time-series land subsidence

Annual line-of-sight (LOS) deformation maps are produced from StaMPS SBAS processing. Fig. 3 highlights the deformation in 2005

calculated with Envisat data (a), the deformation in 2009 calculated with Envisat data (b) and ALOS data (c), and the deformation in 2012 with TerraSAR-X data (d). At least four large subsidence zones can be detected; they are Xi'an High-tech Zone, Xi'an Qujiang New Zone (QJ hereinafter), Chanba River Economic Zone (CBZ hereinafter) and Hujiamiao (HJM hereinafter). With the development of urban construction, Xi'an Hi-tech Zone has the largest subsidence, including three subsidence funnels at Yuhuazhai (YHZ hereinafter), Electronic Mall (EM hereinafter) and Sanyaocun (SYC hereinafter) (Fig. 3). The mean annual displacement at these subsidence zones was about 60 mm. The largest subsidence was found at YHZ: the annual rate increased from 70 mm/a in 2005 to 140 mm/a in 2012.

#### 3.2. InSAR accuracy assessment

The InSAR derived deformation is along the SAR's LOS direction. Assuming that the deformation is purely vertical, all three SAR results are projected into the vertical direction with respect to the corresponding incidence angles. As both Envisat (Fig. 3b) and ALOS SAR (Fig. 3c) images are available in 2009, we compare the vertical displacements during 2009 derived from ALOS and Envisat data processing.

Based on the LOS deformation results in 2009 from ascending ALOS and descending Envisat (Fig. 3b and c), we can see that the deforming areas are generally consistent between the two measurements. Because the spatial distributions of SFP points are different between results derived from two datasets, we have applied the nearest neighbor interpolation to both results before the comparison. After the LOS measurement is converted to the vertical displacement, a common part of the displacement maps (Fig. 3b and c) is selected to compare the vertical deformation measurements between C- and L-band measurements. Fig. 4a shows the difference map while Fig. 4b shows the corresponding histogram. The standard deviation is about 5.5 mm.

In Fig. 4a, larger difference values in the vertical deformation can be seen around fissures and peaks of subsidence areas. Thus the horizontal

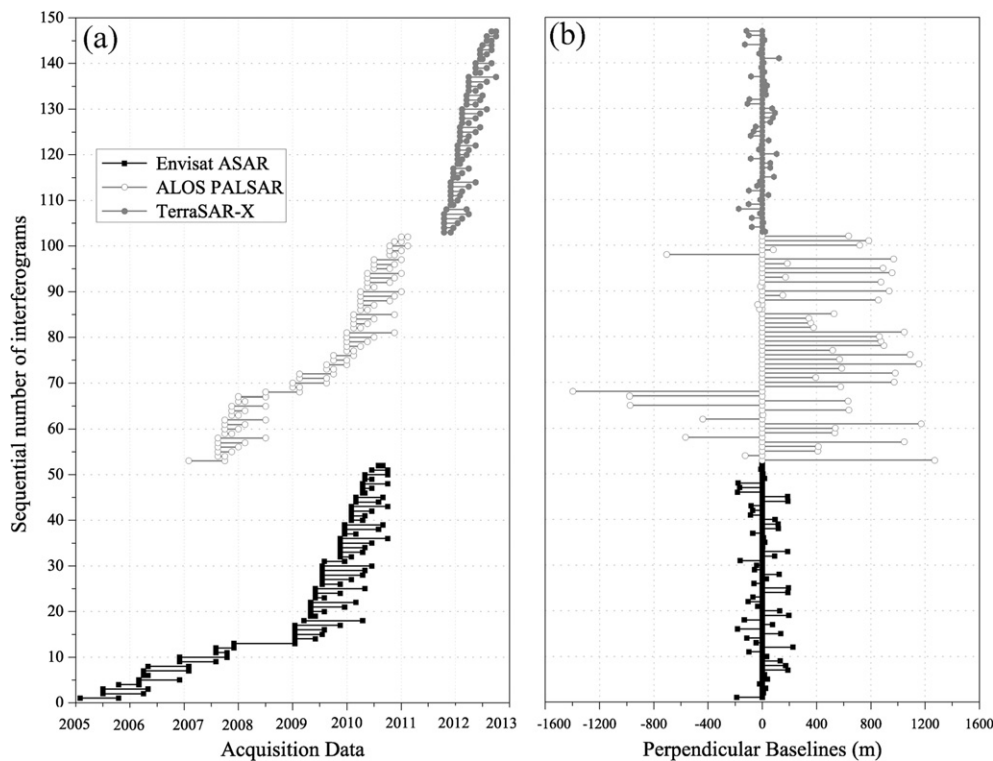


**Fig. 2.** Temporal (a) and perpendicular (b) baseline distributions of SAR interferograms from C-band, L-band and X-band datasets. Black line segments indicate 52 C-band Envisat interferograms with perpendicular baselines less than 250 m and temporal baselines less than 400 days. White line segments represent 50 L-band ALOS interferograms with perpendicular baselines less than 1200 m and temporal baselines less than 350 days. Grey line segments show 45 X-band TerraSAR-X interferograms with perpendicular baselines less than 200 m and temporal baselines less than 200 days.

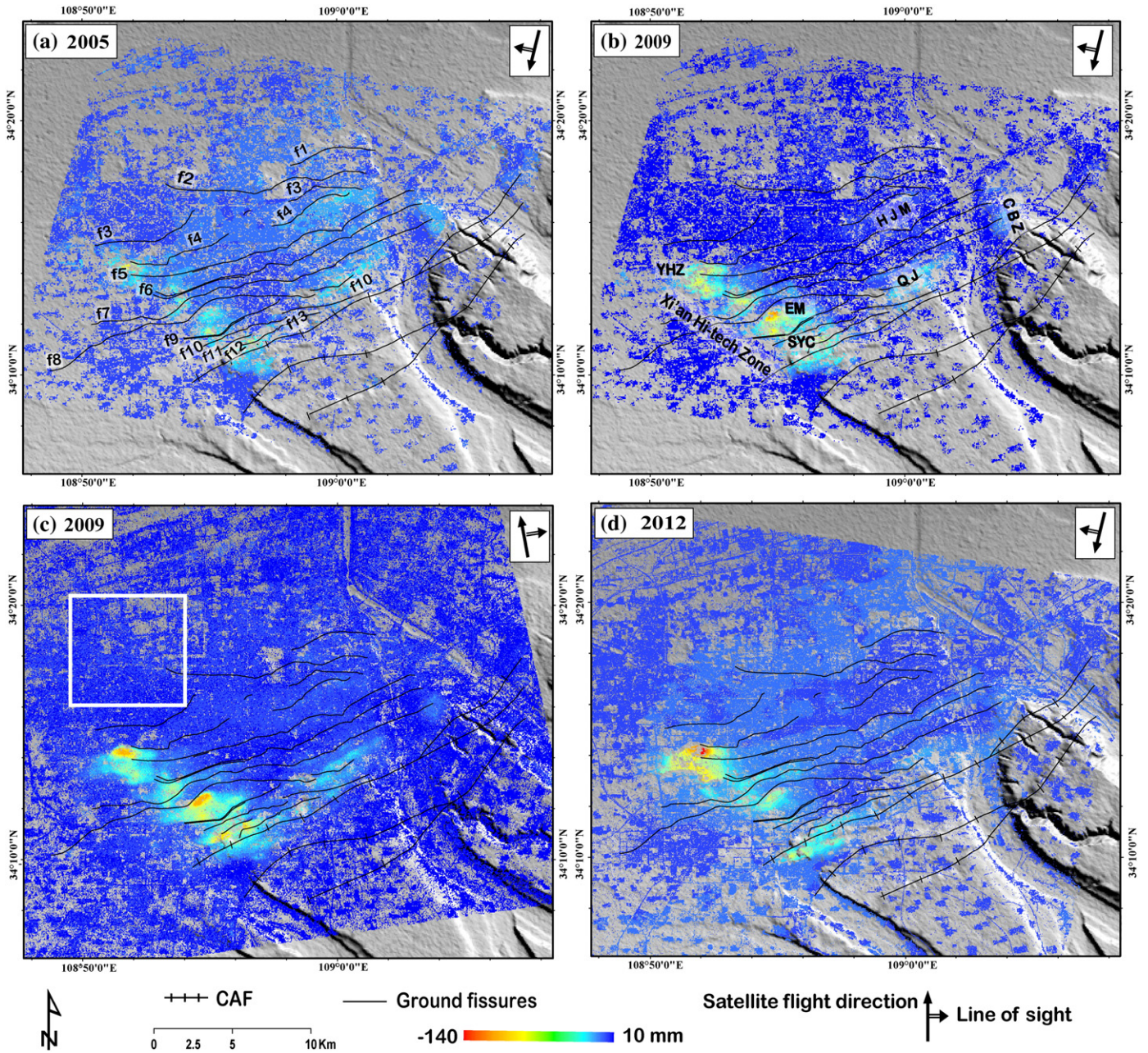


**Fig. 3.** Annual LOS deformation maps of Envisat (a and b), ALOS (c) and TerrSAR-X data (d). Four main large displacement zones are marked in (b): Xi'an Hi-tech Zone, QJ, CBZ and HJM. Three subsidence peaks over the Xi'an Hi-tech Zone are labeled in (b): YHZ, EM and SYC. The white box in (c) indicates the area used to quantify the error level of our InSAR results.

deformation cannot be ignored in these areas. Because both the ascending and descending data are from near-polar orbits, the deformation field in the north–south direction cannot be estimated based on descending and ascending InSAR observations alone (Jung, Lu, Won, Poland, & Miklius, 2011; Samsonov & Tiampo, 2006; Wright, Parsons, & Lu, 2004). Thus the deformation components in the east–west and vertical directions are estimated using the descending and ascending InSAR images together. The measurement equations can be written as:

$$\begin{bmatrix} v_e \\ v_u \end{bmatrix} = U \cdot \begin{bmatrix} d_e \\ d_u \end{bmatrix} - R_{los} \quad (2)$$

where  $d = (d_e, d_u)^T$  is the 2-dimensional deformation vector (east, up) in a local reference frame;  $U$  is a matrix consisting of LOS vectors ( $\sin \theta \cdot \cos \varphi, \cos \theta$ ), where  $\theta$  is the radar incidence angle and  $\varphi$  is the satellite heading angle.  $R$  represents the LOS measurement, and

$(v_e, v_u)$  is the observation residual. By minimizing the observation residual, the deformation vector  $d = -(U^T \cdot U)^{-1} \cdot U^T \cdot R$  is obtained on the basis of least-squares inversion.

The 2-dimensional deformation components are shown in Fig. 5. The vertical displacements (Fig. 5b) range between  $-110$  mm and  $20$  mm, which are much larger than the east–west motions (Fig. 5a). This confirms that the vertical motion dominates the deformation field in Xi'an. Areas with larger east–west displacements correspond to regions of larger vertical displacements where active ground fissures are present (Fig. 5). By comparing Figs. 4a and 5a, we conclude that the horizontal displacements cannot be ignored in land subsidence measurement when the deformation is large, particularly when ground fissures are active.

Next, we compare our InSAR-derived land deformation measurements with GPS and leveling observations (merely the ongoing benchmarks displayed in Fig. 6). To compare the InSAR displacements with

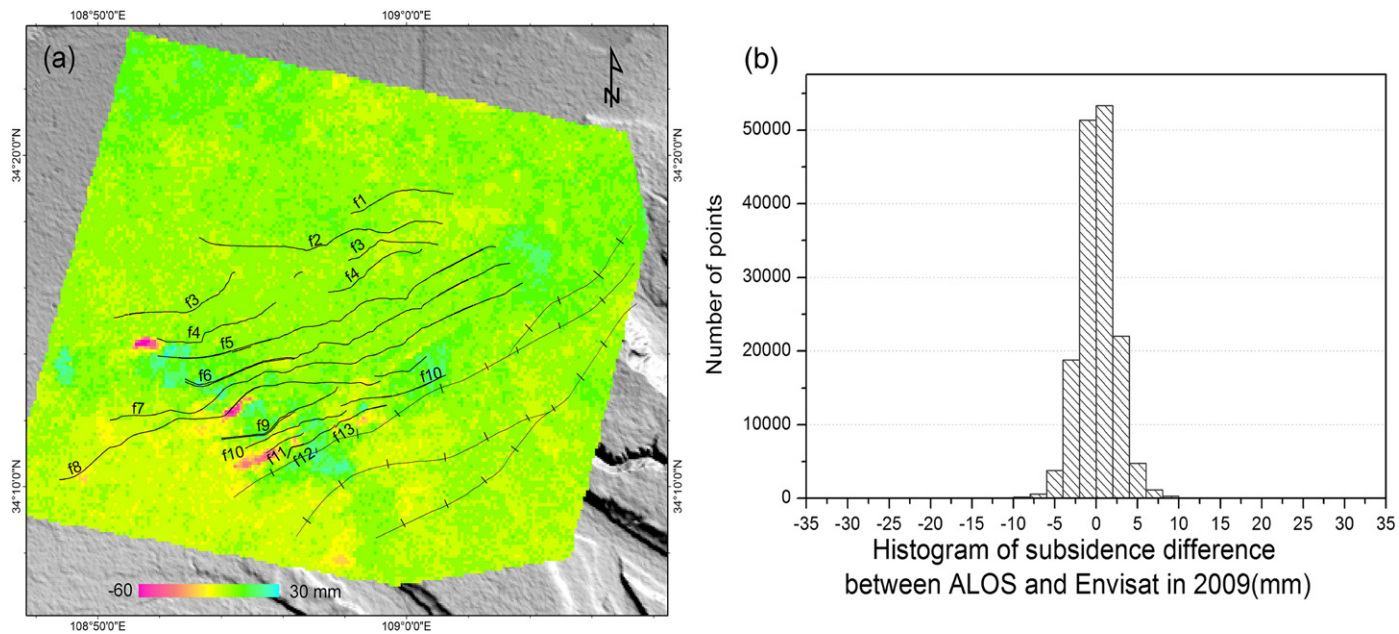


**Fig. 4.** Difference in the vertical displacements derived from ascending ALOS and descending Envisat in 2009 if the observed land deformation is assumed to be vertical. (b) The corresponding histogram of (a).

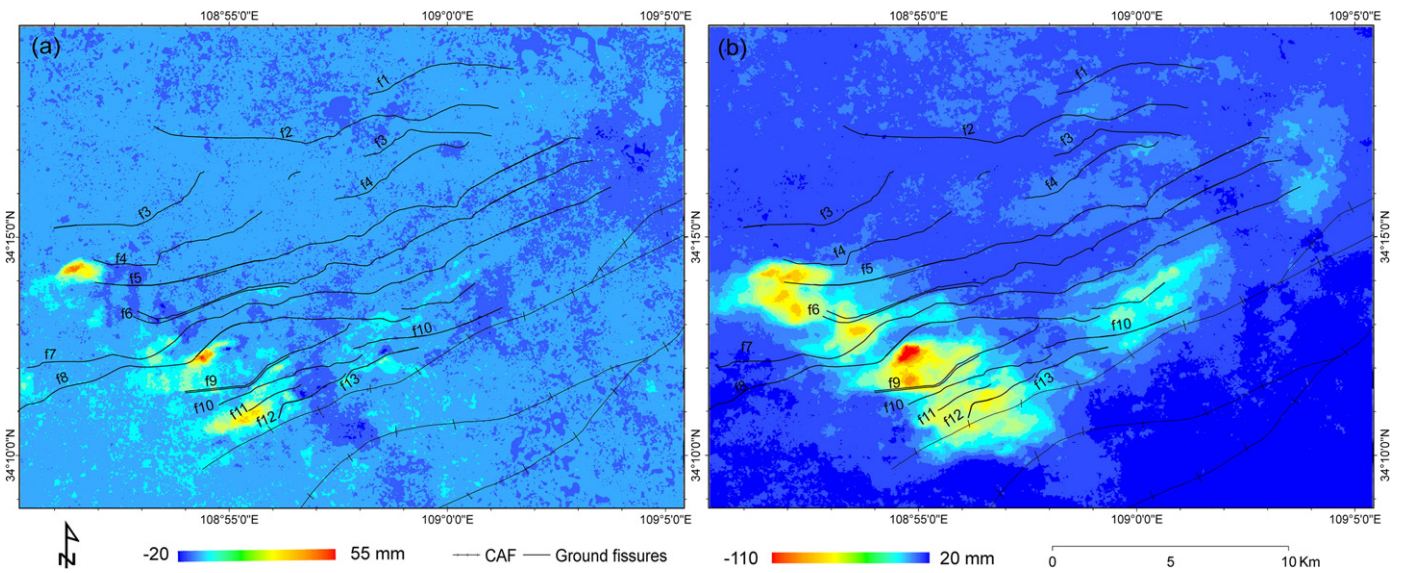


Fig. 5. 2-dimensional deformation map in 2009 by using ascending and descending SAR data: (a) the east–west component of the deformation field; (b) the vertical component of the deformation field.

those from GPS and leveling benchmarks, we select the SFPs that lie within 100 m of benchmarks (for TerrSAR-X the radius distance is set at 50 m as the density of SFP is higher) and average displacement values around benchmarks. After referencing both types of measurements to

the same area and correcting for the offset produced by different time references, we have GPS, leveling and InSAR observations in the same spatial and temporal reference frames. The comparison results (Fig. 6) indicate great agreement between InSAR and GPS/leveling mea-

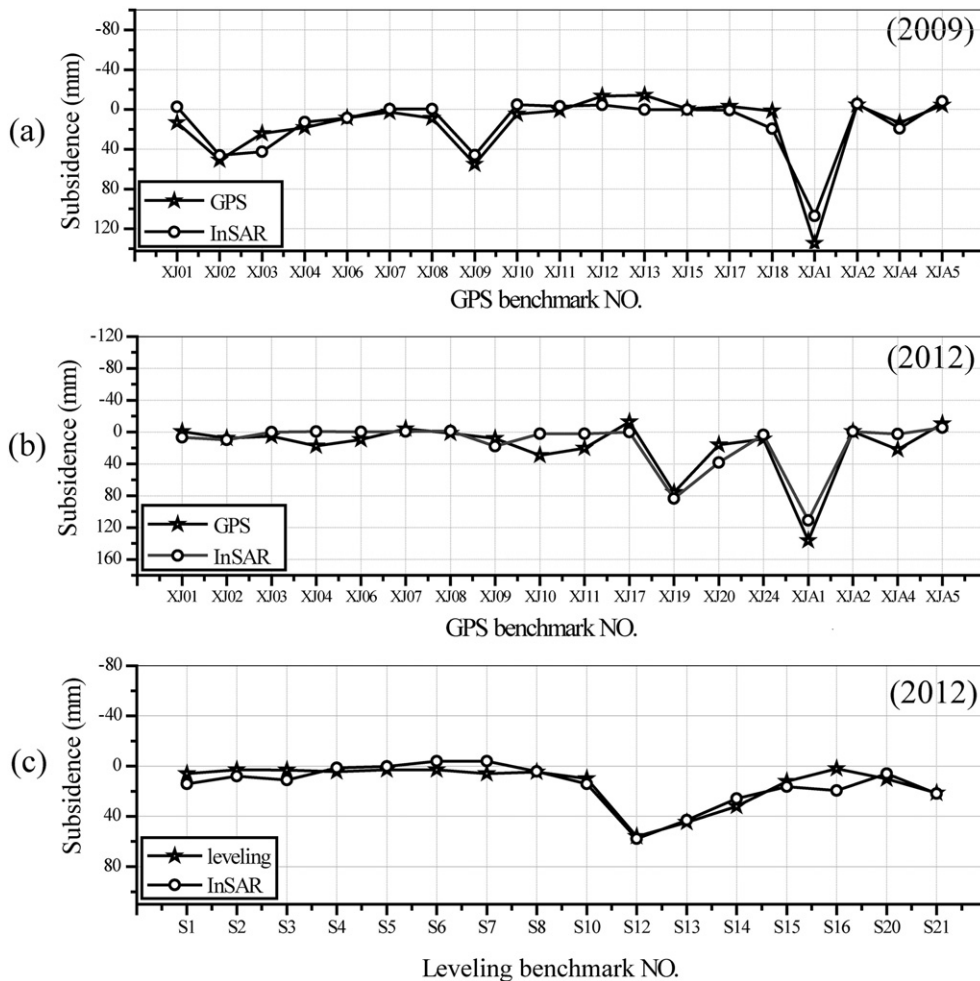


Fig. 6. Comparison of InSAR-derived land surface deformation with those from GPS and leveling measurements. (a) The comparison of InSAR displacement with GPS measurement in 2009. (b) and (c) The comparison of InSAR displacement with GPS and leveling measurements in 2012 respectively.

measurements. Measurements of ground displacement based on individual interferograms can often be overprinted by artifacts due to temporal changes in atmospheric delay and errors in satellite orbit and topographic data used, all of which tend to lower the InSAR accuracy. By using the StaMPS SBAS method described in Section 2.3, we can reduce the atmosphere, baseline and other artifacts efficiently. We calculate the standard deviation of our InSAR measurements over a known nondeforming region (the white box in Fig. 3c) to quantify the precision of our InSAR results. The standard deviation is 3.4 mm/a for the Envisat dataset, 3.1 mm/a for the ALOS, and 2.4 mm/a for the TerraSAR-X.

Discrepancies of up to 30 mm at a few benchmarks (Fig. 6) are likely due to two factors. First, InSAR measurements represent the annual (average) rates from multi-temporal interferograms while GPS and leveling measurements represent deformation measurements between two temporal epochs. So, for benchmarks that experience time-varying displacements (see later discussions), InSAR results will be different from those of GPS and leveling. Second, the larger difference values occur over areas of the greatest deformation gradient. For example, XJ10, XJ11 and XJ12 benchmarks (Fig. 1), which were intended to monitor ground displacements near fissures, are located very close to fissures with spatial separations of less than 50 m. However, only 3 SFPs were identified near these three benchmarks. So, the larger deformation gradient and limited spatial resolution of SFPs have also contributed to the bias. The standard deviations of Fig. 6a and b are 11.7 mm and 15.0 mm, respectively. If the GPS points near ground fissures are excluded, the InSAR precision can reach 8.8 mm and 9.6 mm, respectively (Fig. 6a and b). It is encouraging to see that the InSAR measurement in 2012 is very consistent with the leveling measurement, with a standard deviation of 6.8 mm (Fig. 6c).

### 3.3. Eight years of land subsidence in Xi'an

Fig. 7 shows the cumulative subsidence from 29 January 2005 to 21 September 2012 based on X-, C- and L-band InSAR measurements over the study area. The time-series displacements at four locations (3 are near centers of subsidence cones) are shown in Fig. 8. Because there is a data gap between the last ALOS acquisition (10 February 2011) and the first TerraSAR-X acquisition (5 October 2011), we connect two segments of the time series using average deformation rates during 30 January 2007 to 10 February 2011 (Fig. 8). The maximum cumulative

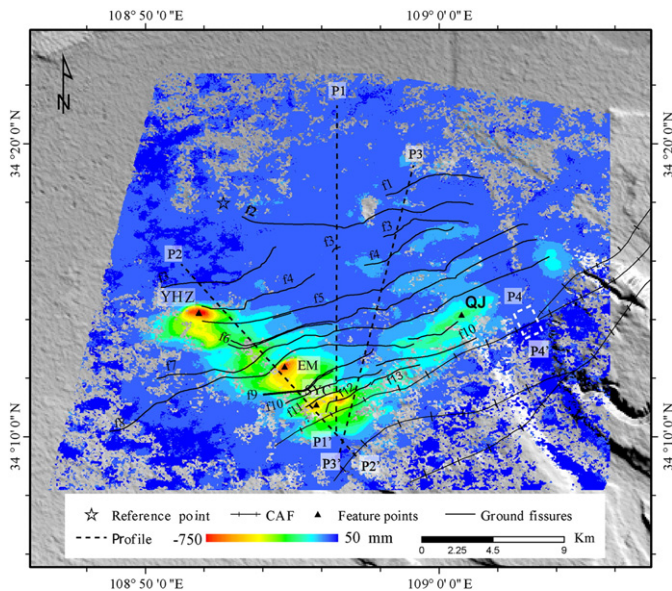


Fig. 7. Cumulative land subsidence map by integrating three InSAR datasets during 2005–2012.

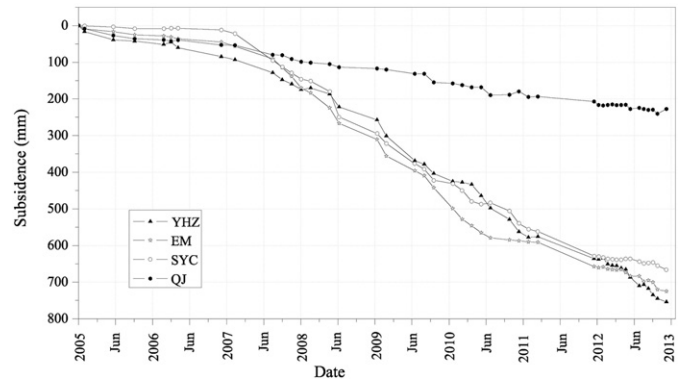


Fig. 8. Time series subsidence of four main subsidence centers including YHZ, EM and SYC over the western Xi'an and QJ in the eastern Xi'an.

subsidence during 2005–2012 is around 740 mm at YHZ and EM, and about 650 mm at SYC. The subsidence rate at QJ remains relatively steady during 2005–2012, and is much lower than those at other three sites, which exhibit time-varying subsidence rates (Fig. 8).

## 4. Discussions

### 4.1. Spatial and temporal variations of land subsidence at Xi'an

Subsidence in Xi'an during 2005–2012 shows strong spatial variations (Fig. 7). The subsidence patterns of each subsiding zone generally are elongated along an ENE direction, following the orientation of fissures and faults in the region. Most of the subsidence zones are confined by fissures in the region (see discussion later). The main subsidence cones are located at the Xi'an High-Tech Zone in western Xi'an, particularly YHZ, EM and SYC (Fig. 7), all of which experienced a significant increase in subsidence rates compared to the measurements in the 1990s (Zhang et al., 2009; Zhao et al., 2008). The maximum subsidence reached about 740 mm at YHZ during 2005–2012 (Fig. 8). Such a significant amount of land subsidence accelerated the development of ground fissures, causing fissures f4 and f5 to extend further westward (Fig. 7). Massive urban structures are under construction in this area, especially Subway Line 3 which will be opened to traffic in 2015. So further attention is required to monitor land subsidence over this area. The land subsidence at EM reached a maximum value of 100 mm/a in 2009, which is almost double the rate during 2005–2007 (Fig. 8). Our InSAR results also reveal changes in spatial distribution of the maximum subsidence over SYC from 2005 to 2012: the maximum subsidence lay to the north of fissure f12 during 2005–2009 (Fig. 3a–c) while it extended to the south of f12 in 2012 (Fig. 3d). Field investigations have identified several small insidious cracks, which have not yet been mapped. Subsidence over the QJ area at southeastern Xi'an is relatively lower than those at YHZ, EM and SYC. Northwestern Xi'an experienced the least subsidence during 2005–2012 (Fig. 7).

Subsidence in Xi'an during 2005–2012 exhibits strong temporal variations (Fig. 8). Over southwestern Xi'an, the subsidence rate increased nearly three times from the period of 2005–2007 to the of period 2008–2010 (Figs. 7 and 8). For example, surface drawdowns over the three main subsidence cones at YHZ, EM, and SYC are about 150 mm during 2005–2007 and about 400 mm during 2008–2010 (Fig. 8). Over southeastern Xi'an, the subsidence maintained a nearly constant rate (Figs. 7 and 8). Frequent temporal sampling of TerraSAR-X images also shows seasonal, nonlinear variations of subsidence. For example, subsidence rates during the period from May to October were larger than those in the other months of 2012 (Fig. 8). These temporal changes in subsidence reflect the variations in ground water pumping (Chang'an University, 2009b).

Comparing our measurements in 2005–2012 with those in the 1990s (Zhang et al., 2009; Zhao et al., 2008, 2009) allows us to evaluate

the changes in spatial and temporal distribution of land subsidence in the past two decades. The main subsidence cones are located at eastern and southern Xi'an, particularly HJM, in the 1990s (Zhang et al., 2009; Zhao et al., 2008, 2009). The maximum subsidence reached about 160 mm in 1992 (Zhang et al., 2009; Zhao et al., 2008, 2009). Peaks of land subsidence moved to southeastern and southwestern Xi'an after 1996 while the subsidence in eastern Xi'an became stabilized. The land subsidence at southwestern Xi'an reached a maximum value of 210 mm/a in 1996 (Zhang et al., 2009; Zhao et al., 2008, 2009), which is almost triple the rate during 2005–2007 and double that of 2008–2012. The main subsidence cones are located at the Xi'an High-Tech Zone in western Xi'an during this period, particularly YHZ, EM and SYC, with a maximum subsidence rate of 140 mm/a in 2012. Overall, the subsidence rate increased from 1992 to 1996, and decreased greatly from 1996 to 2005, and then increased again from 2007. The distribution of land subsidence and ground fissures has gradually migrated from eastern and southern Xi'an to the southwestern suburbs, which can be explained by the expansion of the Xi'an Hi-tech Zone construction in the same period.

#### 4.2. Correlation between land subsidence and groundwater withdrawal

It has been suggested that land subsidence over Xi'an was mainly due to underground water pumping (Wang, 2000; Wang et al., 1996; Zhang, 1990). So ground water withdrawal is the main cause of the observed subsidence presented in this study. An aquifer system is a saturated, heterogeneous body of interbedded permeable and poorly permeable hydrogeologic units consisting of hydraulically-linked aquifers and aquitards. An increase in ground-water pumping causes ground water levels to drop so that some support for the overlying material shifts from the pressurized fluid filling the pore space to the granular skeleton of the aquifer system (e.g., Lu & Danskin, 2001; Sneed, Brandt, & Solt, 2013). As a result of this decrease in pore pressure, the land surface subsides.

Even though the detailed information about groundwater mining in recent years is not publically accessible, we only obtained the ground-water depth along profile P1–P1' (Fig. 7) during 2005 (Chang'an University, 2009b). Accordingly, we compare the observed land subsidence from InSAR during 2005 and the ground water depth along the 20-km-long profile (Fig. 9). There is a strong correlation between the ground settlement and the ground water depth (Fig. 9). The ground subsidence increases with the increase of ground water depth (i.e., decrease of ground water level). The land subsidence spatially coincides with the ground water level drop as a whole, but deviates

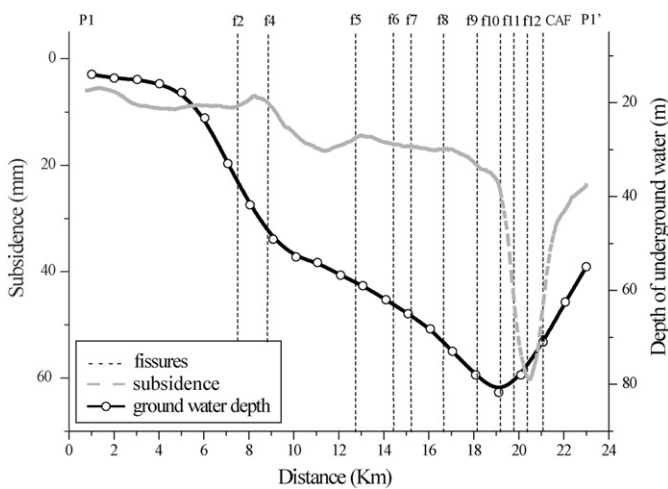


**Fig. 9.** Comparison of InSAR subsidence estimates with the variation of ground water level along profile P1–P1' whose positions are indicated in Fig. 7. Dash lines indicate locations of ground fissures and faults.

locally. The peak subsidence along the profile P1–P1' was near fissure f12, while the maximum water level drop was located about 1 km away. Such an offset is probably due to spatial variations in an aquifer property or the geologic deposits (Chang'an University, 2009b; Lu & Danskin, 2001). For example, the spatial distribution of the clay thickness is one of the important factors affecting land subsidence (Chang'an University, 2009b). Clay is usually thicker in a subsidence center than the surrounding region. A change in clay thickness may cause an inhomogeneity in the spatial distribution of the land subsidence, causing the offset between the peaks of land subsidence and the water level drop.

#### 4.3. Correlation between land subsidence and fissures and faults

Ground fissures in Xi'an are activated as a result of soil surface tension due to land subsidence caused by ground water withdrawal. The shapes of subsiding zones at Xi'an follow the general trend of mapped ground fissures and CAF faults in an ENE direction (Fig. 7). This indicates that the spatial distribution of land subsidence in Xi'an is controlled by faults and fissures to some extent. Fig. 10a and b shows the cumulative surface displacements and their gradients along two profiles (P2–P2', P3–P3'). Major ground fissures and faults are superimposed on the deformation profiles (Fig. 10). Changes in subsidence gradient are

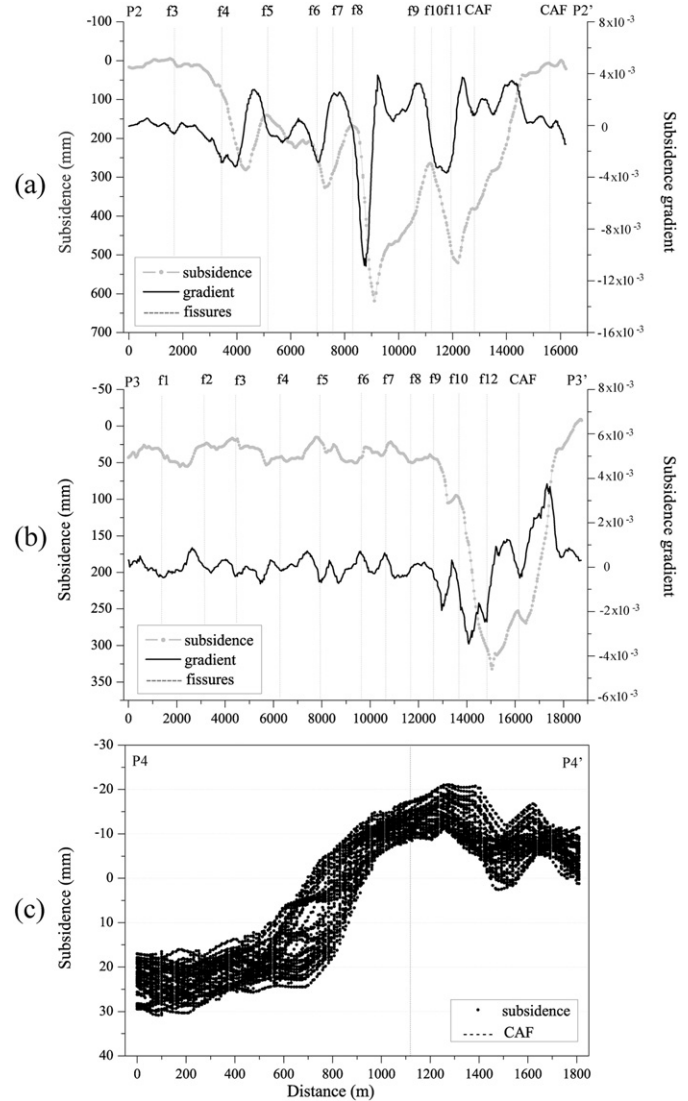


**Fig. 10.** Cumulative land subsidence (2005–2012) and subsidence gradients along three profiles whose positions are marked in Fig. 7. Dash lines indicate locations of ground fissures and faults.

observed over most of the ground fissures and faults, demonstrating a strong correlation between ground fissures and observed subsidence in Xi'an. Two sides of a ground fissure normally have different surface displacements, modifying or weakening the local deformation tendency. On one hand, large localized subsidence gradients destroy the surface tension of soil and promote the relative motion between two blocks of a ground fissure. On the other hand, the formation of ground fissures discontinues the integrity of ground water flow, limits and weakens the horizontal spread of subsidence funnels, and aggravates localized subsidence. Therefore, land subsidence and ground fissures mutually promote each other. Large subsidence gradients, where ground fissures have not been observed, could indicate changes in an aquifer property or geological deposits and might suggest existence of ground water barriers as observed elsewhere (Lu & Danskin, 2001).

Our InSAR results have demonstrated that ground subsidence due to excessive water mining has exacerbated the ground fissures in Xi'an. For example, a significant amount of land subsidence over the YHZ (Fig. 7) accelerated the development of ground fissures, causing fissures f4 and f5 to extend further westward (Chang'an University, 2009a, 2012). Fissure f11 near SYC (Fig. 7) has become one of the most active fractures due to significant localized subsidence. Non-uniform settlements of greater than 20 cm have been observed on both sides of the crack in recent years (Chang'an University, 2009a,b, 2012).

Overall, ground fissure activities correlate with the spatial and temporal variations of ground subsidence. The fissures in the eastern and southern parts of Xi'an were intensively active during 1992–1996, with a creep rate of about 30 mm/a (Zhao et al., 2008, 2009). The fissure activity corresponded well to significant land subsidence occurring over eastern and southern Xi'an during 1992–1996. Fissure activities during 2005–2012 mainly occurred in southwestern Xi'an where the peaks of land subsidence were located (Fig. 7). Take fissure f6 as an example, the eastern section of f6 was not active during 2005–2012, the difference in cumulative subsidence is less than 20 mm (Fig. 10b), which can also be verified by GPS measurements at benchmarks XJ10 and XJ11 (Fig. 6). However this section of f6 moved more than 30 mm/a in the 1990s (Chang'an University, 2009a; Zhang et al., 2009; Zhao et al., 2009, 2008). The western portion of f6 at Xi'an High-tech Zone (Fig. 7), on the other hand, experienced a period of intensified activity during 2005–2012 (Fig. 9a). The difference in the maximum cumulative subsidence reached 120 mm (Fig. 10a). This is in contrast to the fact that there was no deformation at all in the 1990s before the construction of mass infrastructures (Zhang et al., 2009; Zhao et al., 2008, 2009).

Finally, our InSAR results provide a new estimate on the motion of CAF, the major fault system bounding southeastern Xi'an. According to geological investigations (Chang'an University, 2009b; Shi et al., 2008; Zhu et al., 2005, 2006), the CAF is a normal fault dipping to the NNW at an angle of about 66° with a slip rate of about 4 mm/a. Sharp changes in vertical displacement across CAF can be observed in the cumulative subsidence map (white dashed box in Fig. 7) and is highlighted in a cross-section shown in Fig. 10c. The hanging wall (north block) of CAF is in a state of subsidence with a cumulative subsidence of 25 mm while the footwall (south block) uplifts about 10 mm during 2005–2012 (Fig. 10c). So, about 35 mm relative vertical motion in 8 years can be interfered from our InSAR analysis, resulting in a slip rate of 4 mm per year along the fault plane (i.e.,  $35 \text{ mm}/8 \text{ year}/\sin(66^\circ)$ ). Our results therefore agree well with the geological observation.

## 5. Conclusions

Using C-, L- and X-band InSAR imagery acquired during 2005–2012, we unveil the spatial and temporal variations of land subsidence and ground fissures in Xi'an. Combining InSAR results, GPS and level observations, and measurements of the ground water level of aquifers, we can draw the following conclusions. First, using GPS and leveling observations, we report that the precision of our InSAR annual subsidence results can reach 9 mm. Combining descending and ascending InSAR

observations, we have derived the east–west and vertical components of the observed land deformation. The horizontal component of land deformation can't be ignored if the deformation is large or ground fissures are active. This provides a cautionary implication for comparing InSAR LOS deformation measurements from different geometries. Second, four main land subsidence zones are detected at the Xi'an Hi-tech Zone, Xi'an Qujiang New Zone, Chanba River Economic Zone and Hujiamiao, with an average subsidence rate of about 50 mm/a during 2005–2012. The peak land subsidence is found in the Xi'an Hi-tech Zone in western Xi'an, where subsidence rates reached 140 mm/a in 2012. Land subsidence rates over Xi'an increased by 200% from 2005–2007 to 2008–2012, extending existing ground fissures. Third, InSAR-derived land subsidence correlates with the change in ground water level: the larger the ground water-level drop, the larger the observed subsidence. Seasonal, nonlinear variations of subsidence observed from the more frequently sampled TerraSAR-X images suggest that subsidence rates from May to October were larger than those in the other months of 2012, which reflects variations in ground water pumping. Fourth, the shapes of subsiding zones follow the general trends of mapped ground fissures and main faults in an ENE direction. Ground fissures are activated by horizontal strain generated by the bending of overburden in response to localized differential land subsidence. Accordingly, changes in subsidence gradients are observed over most of the ground fissures and faults. Presence of fissures can induce localized surface displacements, aggravate localized subsidence, discontinue the integrity of ground water flow, and limit the horizontal spread of subsidence funnels. Therefore, spatial–temporal variations in land subsidence correlate with activities of ground fissures, and they mutually promote each other.

With the enormous urban sprawl and mass construction in Xi'an, monitoring ground deformation with satellite InSAR can provide a precise and economic means to image land subsidence and movements of fissures and faults and the associated geohazards. Not only is it a great way to image the characteristics of spatial–temporal evolution and mechanism of land subsidence and ground fissures, but it also provides independent unparalleled data for the further geological and geophysical interpretation. It is eventually enhancing disaster prevention and mitigation, which is essential for protecting people's lives and property.

Our future study will continue the monitoring of land subsidence in Xi'an using multiple radar satellites including Sentinel-1/A, Radarsat-2, COSMO-SkyMed and ALOS-2. With SAR acquisitions from multiple sensors with different imaging geometries, an advanced multi-interferogram time-series analysis technique based on Helmert variance component estimation will be developed to improve the accuracy of InSAR measurements. Multifarious observations can also enhance the accuracy of deformation decomposition to generate precise 3-dimensional deformation components. Furthermore, additional continuous GPS stations will soon be included to improve the validation of our InSAR results.

## Acknowledgments

This research is funded by projects of the Natural Science Foundation of China (NSFC) (Project Nos: 41274004, 41274005, 41304016, 41372375 and 41202189), the Special Fund for Basic Scientific Research of Central Colleges (Grant No. 2013G5260004, Chang'an University), also by the project of the Ministry of Land & Resources, China (Project No: 1212011220186). Feifei Qu would also like to thank the China Scholarship Council for funding her study at Southern Methodist University. Zhong Lu is supported by the Shuler–Foscue Endowment at Southern Methodist University and NASA's Earth Surface & Interior Program. Three arc-seconds SRTM DEM are freely downloaded from the website <http://rmw.recordist.com/index.html>. Thanks to the excellent software package StaMPS, which can be freely downloaded from the website <http://homepages.see.leeds.ac.uk/~earahoo/stamps/index.html>.

## References

- Amelung, F., Galloway, D. L., Bell, J., Zebker, H. A., & Laczniak, R. (1999). Sensing the ups and downs of Las Vegas: InSAR reveals structural control of land subsidence and aquifer-system deformation. *Geology*, 27(6), 483–486.
- Bawden, G. W., Thatcher, W., Stein, R. S., Hudnut, K. W., & Peltzer, G. (2001). Tectonic contraction across Los Angeles after removal of groundwater pumping effects. *Nature*, 412, 812–815.
- Berardino, P., Fornaro, G., Lanari, R., & Sansosti, E. (2002). A new algorithm for surface deformation monitoring based on small baseline differential interferograms. *IEEE Transactions on Geoscience and Remote Sensing*, 40(11), 2375–2383.
- Burbey, T. (2002). The influence of faults in basin-fill deposits on land subsidence, Las Vegas Valley, Nevada, USA. *Hydrogeology Journal*, 10(5), 525–538.
- Chang'an University (2009a). *Monitoring land subsidence and ground fissures over Fenwei basin by using InSAR and GPS techniques*. (Xi'an, Shaanxi province, China (in Chinese)).
- Chang'an University (2009b). *Thematic study of the monitoring and control of the land subsidence and ground fissure in Fenwei basin*. (Xi'an, Shaanxi province, China (in Chinese)).
- Chang'an University (2012). *Monitoring land subsidence and ground fissures over Fenwei basin by using InSAR and GPS techniques*. (Xi'an, Shaanxi province, China (in Chinese)).
- Ding, X. L., Liu, G. X., Li, Z. W., Li, Z. L., & Chen, Y. Q. (2004). Ground subsidence monitoring in Hong Kong with satellite SAR interferometry. *Photogrammetric Engineering & Remote Sensing*, 70(10), 1151–1156.
- Ferretti, A., Fumagalli, A., Novati, F., Prati, C., Rocca, F., & Rucci, A. (2011). A new algorithm for processing interferometric data-stacks: SqueeSAR. *IEEE Transactions on Geoscience and Remote Sensing*, 49(9), 3460–3470.
- Ferretti, A., Prati, C., & Rocca, F. (2001). Permanent scatterers in SAR interferometry. *IEEE Transactions on Geoscience and Remote Sensing*, 39(1), 8–20.
- Fruneau, B., & Sarti, F. (2000). Detection of ground subsidence in the city of Paris using radar interferometry: Isolation of deformation from atmospheric artifacts using correlation. *Geophysical Research Letters*, 27(24), 3981–3984.
- Heleno, S. I. N., Oliveira, L. G. S., Henriques, M. J., Falcão, A. P., Lima, J. N. P., Cooksley, G., et al. (2011). Persistent scatterers interferometry detects and measures ground subsidence in Lisbon. *Remote Sensing of Environment*, 115(8), 2152–2167.
- Hoffmann, J., Zebker, H. A., & Galloway, D. L. (2001). Seasonal subsidence and rebound in Las Vegas Valley, Nevada, observed by synthetic aperture radar interferometry. *Water Resources Research*, 37(6), 1551–1566.
- Hooper, A. (2006). *Persistent scatterer radar interferometry for crustal deformation studies and modeling of volcanic deformation* (PhD thesis).
- Hooper, A. (2008). A multi-temporal InSAR method incorporating both persistent scatterer and small baseline approaches. *Geophysical Research Letters*, 35, L16302, <http://dx.doi.org/10.1029/2008GL034654>.
- Hooper, A., Segall, P., & Zebker, H. (2007). Persistent scatterer InSAR for crustal deformation analysis, with application to Volcán Alcedo, Galapagos. *Journal of Geophysical Research*, 112, B07407.
- Hooper, A., & Zebker, H. (2007). Phase unwrapping in three dimensions with application to InSAR time series. *Journal of the Optical Society of America A. Optics and Image Science*, 24, 2737–2747.
- Hooper, A., Zebker, H., Segall, P., & Kampes, B. (2004). A new method for measuring deformation on volcanoes and other natural terrains using InSAR persistent scatterers. *Geophysical Research Letters*, 31(23), 611–615.
- Joaquim, J. S., Hooper, A., Hanssen, R., Bastos, L., & Ruiz, A. (2011). Persistent Scatterer InSAR: A comparison of methodologies based on a model of temporal deformation vs. spatial correlation selection criteria. *Remote Sensing of Environment*, 115, 2652–2663.
- Jung, H. S., Lu, Z., Won, J., Poland, M., & Miklius, A. (2011). Mapping three-dimensional surface deformation by combining multiple aperture interferometry and conventional interferometry: application to the June 2007 eruption of Kilauea Volcano, Hawaii. *IEEE Geoscience & Remote Sensing Letters*, 8(1), 34–38.
- Kampes, K., Hanssen, R., & Perski, Z. (2003). Radar interferometry with public domain tools. *Proceedings of FRINGE 2003*. Frascati, Italy: ESA SP-550.
- Lanari, R., Mora, O., Manunta, M., Mallorqui, J. J., Berardino, P., & Sansosti, E. (2004). A small-baseline approach for investigating deformations on full-resolution differential SAR interferograms. *IEEE Transactions on Geoscience and Remote Sensing*, 42, 1377–1386.
- Lee, C. W., Lu, Z., Jung, H. S., Won, J. S., & Dzurisin, D. (2010). Surface deformation of Augustine Volcano (Alaska), 1992–2005, from multiple-interferogram processing using a refined SBAS InSAR approach. chapter 18 of. In J. A. Power, M. L. Coombs, & J. T. Freymueller (Eds.), *The 2006 eruption of Augustine Volcano, Alaska*. U.S. Geological Survey Professional Paper, 1769. (pp. 453–465).
- Lee, C. F., Zhang, J. M., & Zhang, Y. X. (1996). Evolution and origin of the ground fissures in Xi'an, China. *Engineering Geology*, 43, 45–55.
- Lu, Z., & Danskin, W. (2001). InSAR analysis of natural recharge to define structure of a ground-water basin, San Bernardino, California. *Geophysical Research Letters*, 28, 2661–2664.
- Lu, Z., & Dzurisin, D. (2014). *InSAR imaging of Aleutian volcanoes: Monitoring a volcanic arc from space*. Springer Praxis Books, Geophysical Sciences 978-3-642-00347-9 (390 pp.).
- Lu, Z., Dzurisin, D., Jung, H. S., Zhang, J. X., & Zhang, Y. H. (2010). Radar image and data fusion for natural hazards characterization. *International Journal of Image and Data Fusion*, 1, 217–242.
- Lu, Z., Patrick, M., Fielding, E. J., & Trautwein, C. (2003). Lava volume from the 1997 eruption of Okmok volcano, Alaska, estimated from spaceborne and airborne interferometric synthetic aperture radar. *IEEE Transactions on Geoscience and Remote Sensing*, 41, 1428–1436.
- Lu, Z., & Zhang, L. (2014). Frontiers of radar remote sensing. *Photogrammetric Engineering & Remote Sensing*, 80(1), 5–13.
- Massonnet, D., Rossi, M., Carmona, C., Adragna, F., Peltzer, G., Feigl, K., et al. (1993). The displacement field of the Landers earthquake mapped by radar interferometry. *Nature*, 364(6433), 138–142.
- Mora, O., Mallorqui, J. J., & Broquetas, A. (2003). Linear and nonlinear terrain deformation maps from a reduced set of interferometric SAR images. *IEEE Transactions on Geoscience and Remote Sensing*, 41(10), 2243–2253.
- Osmanoglu, B., Dixon, T. H., Wdowinski, S., Cabral-Cano, E., & Jiang, Y. (2011). Mexico City subsidence observed with persistent scatterer InSAR. *International Journal of Applied Earth Observation and Geoinformation*, 13(1), 1–12.
- Peltzer, G., & Rosen, P. (1995). Surface displacement of the 17 May 1993 Eureka Valley, California, earthquake observed by SAR interferometry. *Science*, 268(5215), 1333–1336.
- Peng, J. B., Su, S. R., & Zhang, J. (1992). *The active faults and geohazards in Weihe basin*. Xi'an: Northwest University Press (in Chinese).
- Perissin, D., & Wang, T. (2010). Time-series InSAR applications over urban areas in China. *IEEE Journal of Selected Topics in Applied Earth Observations and Remote Sensing*, 4(1), 92–100.
- Samsonov, S., & Tiampo, K. (2006). Analytical optimization of DInSAR and GPS dataset for derivation of three-dimensional surface motion. *IEEE Geoscience and Remote Sensing Letters*, 3(1), 107–111.
- Schmidt, D. A., & Bürgmann, R. (2003). Time dependent land uplift and subsidence in the Santa Clara Valley, California, from a large InSAR data set. *Journal of Geophysical Research*, 108(B9).
- Shi, Y. Q., Feng, X. J., Dai, W. Q., Li, X. N., Ren, J., & Chong, J. (2008). Geometric structure and formation mechanism of Lintong–Changan fault zone. *Acta Seismologica Sinica*, 30(2), 152–164 (in Chinese).
- Sneed, M., Brandt, J., & Solt, M. (2013). Land subsidence along the Delta-Mendota Canal in the northern part of the San Joaquin Valley, California, 2003–10. *U.S. Geological Survey Scientific Investigations Report 2013-5142*, <http://dx.doi.org/10.3133/sir20135142> (87 pp.).
- Suo, C. M., Wang, D. Q., & Liu, Z. Z. (2005). Land fracture and subsidence prevention in Xi'an. *Quaternary Research*, 25(1), 23–28 (in Chinese).
- Tesaro, M., Berardino, P., Lanari, R., Sansosti, E., Fornaro, G., & Franceschetti, G. (2000). Urban subsidence inside the city of Napoli (Italy) observed by satellite radar interferometry. *Geophysical Research Letters*, 27(13), 1961–1964.
- Wang, J. M. (2000). *Theory of ground fissures hazards and its application*. Xi'an: Shaanxi Science and Technology Press (in Chinese).
- Wang, D. Q., Suo, C. M., & Jia, S. J. (1996). A quantitative analysis of recently extraordinary movement factors of geofractures in Xi'an. *Geology of Shaanxi*, 14(1), 49–58 (in Chinese).
- Wegmuller, U., Walter, D., Spreckels, V., & Werner, C. (2010). Nonuniform ground motion monitoring with TerraSAR-X persistent scatterer interferometry. *IEEE Transactions on Geoscience and Remote Sensing*, 48(2), 895–904.
- Werner, C., Wegmuller, U., Strozzi, T., & Wiesmann, A. (2003). Interferometric point target analysis for deformation mapping. *Paper presented at International Geoscience and Remote Sensing Symposium*. Toulouse, France: Geosci. & Remote Sens. Soc.
- Wright, T. J., Parsons, B. E., & Lu, Z. (2004). Toward mapping surface deformation in three dimensions using InSAR. *Geophysical Research Letters*, 31, L01607, <http://dx.doi.org/10.1029/2003GL018827>.
- Xi'an City Planning Bureau (2006). *Regulations of field reconnaissance and engineering design of Xi'an ground fissures*. Institute of Geotechnical Investigation and Design MMI and China Northwest Building Design Research Institute. Xi'an, China: Xi'an City Planning Bureau (No. DBJ61-6-2006).
- Xi'an Local Records Compilation Committee (1996). *Xi'an local records*. Xi'an: Xi'an Publishing House ((in Chinese). ISBN 7-80594-277-3/C.8. ([http://www.sxsdq.cn/dqzlk/dfz\\_sxz/xasz\\_1/](http://www.sxsdq.cn/dqzlk/dfz_sxz/xasz_1/))).
- Yan, W. Z. (1998). Analysis on the origin of land subsidence and its countermeasures of control in Xi'an. *Chinese Journal of Geological Hazard and Control*, 119, 27–32 (in Chinese).
- Yan, W. Z. (1999). Xi'an ground fissures map, in Shaanxi Geology and minerals resources bureau, Shaanxi proposal committee. *Xi'an environmental geological atlas*. Xi'an: Xi'an Mapping Press (in Chinese).
- Zebker, H. A., Rosen, P. A., Goldstein, R. M., Gabriel, A., & Werner, C. L. (1994). On the derivation of coseismic displacement fields using differential radar interferometry: The Landers earthquake. *Journal of Geophysical Research*, 99, 19617–19634.
- Zebker, H. A., & Villaseno, J. (1992). Decorrelation in interferometric radar echoes. *IEEE Transactions on Geoscience and Remote Sensing*, 30(5), 950–959.
- Zhang, J. M. (1990). *Research on ground fracture in the region of Xi'an*. Xi'an: Northwest University Press (in Chinese).
- Zhang, Q., Zhao, C. Y., Ding, X. L., Chen, Y. Q., Wang, L., Huang, G. W., et al. (2009). Research on recent characteristics of spatio-temporal evolution and mechanism of Xi'an land subsidence and ground fissure by using GPS and InSAR techniques. *Chinese Journal of Geophysics*, 52(5), 1214–1222.
- Zhao, C. Y., Zhang, Q., Ding, X. L., Lu, Z., Yang, C. S., & Qi, X. M. (2009). Monitoring of land subsidence and ground fissures in Xi'an, China 2005–2006: mapped by SAR interferometry. *Environmental Geology*, 58, 1533–1540.
- Zhao, C. Y., Zhang, Q., Ding, X. L., Peng, J. B., & Yang, C. S. (2008). InSAR based evaluation of land subsidence and ground fissure evolution at Xi'an. *Journal of Engineering Geology*, 17(3), 389–393.
- Zhu, Y. Q., Cheng, H. B., & Jiang, Z. S. (2005). The tectonic deformation and segmented features of Lintong–Changan fracture zone. *Earthquake Research in Plateau*, 17(3), 18–26 (in Chinese).
- Zhu, Y. Q., Wang, Q. L., Tian, Q. J., Liang, W. F., & Zhang, X. L. (2006). Comprehensive analysis and study of crustal deformation in Guanzhong area. *Journal of Geodesy and Geodynamics*, 26(4), 56–62 (in Chinese).
- Zhuang, J. Q., Javed, I., Peng, J. B., & Liu, T. M. (2014). Probability prediction model for landslide occurrences in Xi'an, Shaanxi Province, China. *Journal of Mountain Science*, 11(2), 345–359.